Fatigue crack growth resistance of the austenitic stainless steel Alloy 709 at elevated temperatures

Yu, Suyang; Yan, Jin; Li, Hangyue; Ding, Rengen; Lall, Amrita; Rabiei, Afsaneh; Bowen, Paul

DOI:
10.1016/j.jmrt.2020.09.050

Document Version
Publisher's PDF, also known as Version of record

Citation for published version (Harvard):
Yu, S, Yan, J, Li, H, Ding, R, Lall, A, Rabiei, A & Bowen, P 2020, 'Fatigue crack growth resistance of the austenitic stainless steel Alloy 709 at elevated temperatures', *Journal of Materials Research and Technology*, vol. 9, no. 6, pp. 12955-12969. https://doi.org/10.1016/j.jmrt.2020.09.050

J MATER RES TECHNOL. 2020;9(6):12955–12969

Available online at www.sciencedirect.com

jmr&t Journal of Materials Research and Technology

https://www.journals.elsevier.com/journal-of-materials-research-and-technology

Original Article

Fatigue crack growth resistance of the austenitic stainless steel Alloy 709 at elevated temperatures

Suyang Yu[a,*], *Jin Yan*[a], *Hangyue Li*[a], *Rengen Ding*[a], *Amrita Lall*[b], *Afsaneh Rabiei*[b], *Paul Bowen*[a]

[a] *School of Metallurgy and Materials, College of Engineering and Physical Sciences, University of Birmingham, Edgbaston, Birmingham, B15 2TT, UK*

[b] *Department of Mechanical and Aerospace Engineering, North Carolina State University, 911 Oval Dr, Raleigh, NC 27695-7910, USA*

ARTICLE INFO

Article history:
Received 16 July 2020
Accepted 10 September 2020
Available online 24 September 2020

Keywords:
Alloy 709
Fatigue crack growth
In-Situ testing
FIB-TEM
Environmental effect

ABSTRACT

Fatigue crack growth resistance of an austenitic stainless steel Alloy 709 has been evaluated at temperatures of 550, 650 and 750 °C in air and vacuum. Tests were conducted at a frequency of 0.25 Hz and a stress ratio of 0.1. The linear elastic stress intensity factor range (ΔK) has been used to characterise fatigue crack growth resistance. A modest detrimental effect of air at elevated temperatures on fatigue crack growth is identified and discussed. Striated transgranular fatigue is found to be the failure mechanism for all test conditions. The formation of striations and the interaction of crack growth with slip traces are further investigated using in-situ testing (within a scanning electron microscope), together with transmission electron microscopy carried out on samples extracted by focused ion-beam milling perpendicular to fracture surfaces. Finally, an analytical model is proposed to predict fatigue crack growth in air for Alloy 709.

1. Introduction

A drive towards improved reactor economics, greater safety margins and design flexibility has led to the development of Sodium-cooled Fast Reactors (SFRs). Alloy 709 has been developed by Oak Ridge National Laboratory for use in SFRs based on NF709 (a steel developed by Nippon Steel Corporation [1]). Applications for hot sections in SFRs require a longer design lifetime and hence sufficient creep and fatigue properties are needed. A realistic approach requires consideration of the possibility of fracture originating from existing structural flaws. Information on the rate at which a flaw or small crack may grow to a critical size is necessary to predict safe operating periods. For this relatively new grade of material, such information of crack growth rates is yet limited. In terms of fatigue crack growth in Alloy 709, there is only one study made by N. Shaber et al. [2] on fatigue crack growth rates at high temperatures in air environment, which mainly focused on the mechanical behaviour of the material.

In sodium-cooled fast reactors, some structural material will be exposed to liquid sodium. Previous research on the fatigue behaviour of 316 stainless steel shows that at the temperature of 625 °C the endurance of the material in high purity sodium was up to five times greater than that in air [3]. M.P. Mishra et al. tested 316 L N (a low carbon, nitrogen-enhanced version of 316 stainless steel) in air, argon and liquid sodium

* *Corresponding author.*
E-mail: s.s.yu@bham.ac.uk (S. Yu).

https://doi.org/10.1016/j.jmrt.2020.09.050

environment at 540 °C and found that fatigue crack growth rates are considerably slower in both argon and sodium than in air [4], which suggests that the sodium environment can essentially be regarded as an inert environment. Hence an evaluation of crack growth resistance in a quasi "oxygen-free" environment is also desirable.

This paper considers the fatigue crack growth resistance of Alloy 709 and later papers consider dwell fatigue crack growth and creep crack growth. The current study focuses on the evaluation of fatigue crack growth resistance of Alloy 709 at elevated temperatures in both air and vacuum environment using a linear elastic fracture mechanics (LEFM) approach. Not only useful crack growth data were generated with conventional testing using Compact Tension (CT) testpieces, in-situ mechanical testing within a scanning electron microscope (SEM) and transmission electron microscopy (TEM) characterization performed on samples extracted using focused ion beam milling within a scanning electron microscope (FIB-SEM) were also conducted to provide in-depth understanding of fatigue crack growth mechanisms of austenitic stainless steels at high temperatures. Furthermore, an analytical model is proposed to address the environmental effect of air on fatigue crack growth rates in Alloy 709 at elevated temperatures.

2. Experimental

2.1. Material and testpiece

Alloy 709 stainless steel examined in the current research is provided by Argonne National Laboratory. The nominal chemical composition (wt%) of the alloy is given in Table 1. As-received material was firstly hot rolled and then annealed at 1100 °C for 2 h, followed by water-quenching.

CT testpieces with a width of 26 mm and a thickness of 13 mm were machined from two plates provided which had a thickness of 20 and 32 mm respectively. Side-grooves of 0.5 and 1 mm depth (each side) were machined in some testpieces. The material in the 20 mm thick plate has equiaxed austenitic grains with an average size of 48 μm. Detailed studies of the microstructure of Alloy 709 from this 20 mm thick plate and its tensile properties at 550, 650 and 750 °C can be found in previous work [5–7]. Four testpieces, A1-A4, extracted from this plate are considered here. Due to the limited thickness of this plate, only CT testpieces with the L-T orientation (crack growth direction being parallel to the transverse direction and crack plane being perpendicular to the rolling direction) were extracted.

The microstructure of material in the 32 mm thick plate fell outside of the required specification as it comprised an inhomogeneous banded mixture of coarse and fine austenitic grains, although it had been subjected to similar processing and heat treatment. Optical micrographs of the material from these two plates are given in Fig. 1. Because of its larger thickness, CT testpieces with the ST-L orientation (crack growth direction being parallel to the rolling direction and crack plane being perpendicular to the short-transverse direction) were also machined from this plate in addition to the L-T orientation to explore the potential influence of this inhomogeneous microstructure and testpiece orientation. Seven testpieces, B1-B7, extracted from this plate are considered here.

2.2. Fatigue crack growth resistance tests

Fatigue crack growth resistance tests were conducted both in air and in vacuum at temperatures of 550, 650 and 750 °C following procedures given in ASTM E647 [8]. First, all testpieces were fatigue precracked at room temperature using an Amsler Vibrophore at a frequency of ~ 80 Hz and a stress ratio R of 0.1 ($R = K_{min}/K_{max}$). After precracking, testpieces were transferred to a servo-electric mechanical testing machine for all air tests. A resistance furnace was used to achieve and to maintain the test temperature (to ±2 °C) during fatigue crack growth testing. Vacuum tests were conducted using an ESH

Table 1 – Chemical composition of Alloy 709.

Element	Ni	Cr	Nb	Mn	Mo	N	Si	B	C	S	Ti	P	Fe
Composition (wt%)	25.00	19.69	0.23	0.88	1.46	0.14	0.28	0.0022	0.063	< 0.001	< 0.01	< 0.005	Balance

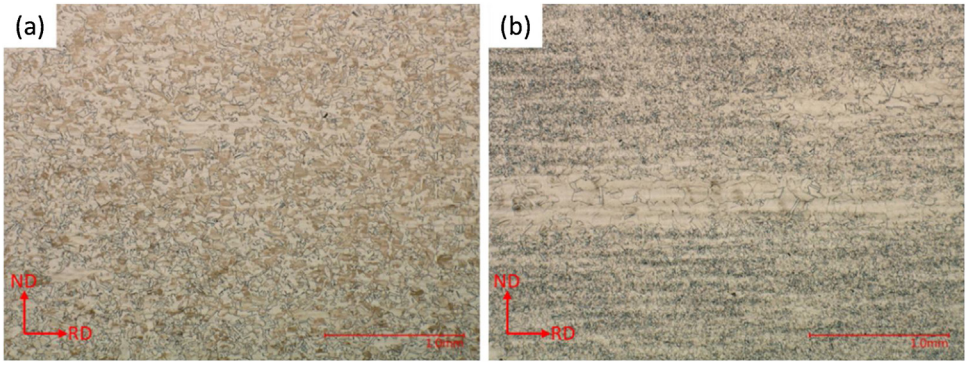

Fig. 1 – Optical micrographs of Alloy 709 derived from two hot-rolled plates used in the current research. (a) equiaxed grain structure acquired from a 20 mm thick plate and (b) off-specification banded microstructure acquired from a 32 mm thick plate.

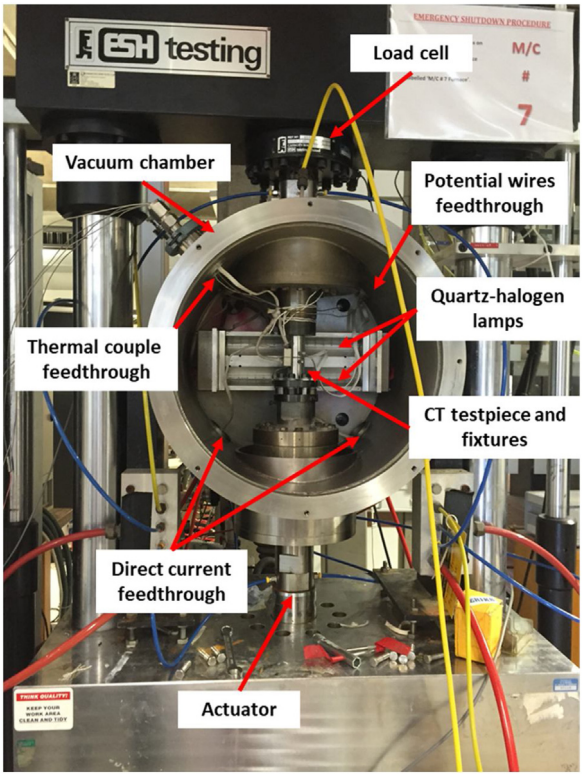

Fig. 2 – Photo showing the mechanical testing machine used for vacuum tests at elevated temperatures. Note that the front door is not shown in this photo to reveal the inside of the vacuum chamber.

servo-hydraulic mechanical testing machine equipped with a vacuum chamber. A photo of this system is shown in Fig. 2. Testpieces were heated by four quartz-halogen lamps and a vacuum of ~1.5×10^{-5} mbar was generally achieved. Note that only two lamps are visible in Fig. 2 whereas the other two are attached to the front door of the vacuum chamber which is not shown in this photo. A 0.25 Hz sinusoidal load waveform with a constant stress range and R = 0.1 were used for both air and vacuum tests. Therefore, the stress intensity factor range (ΔK) increases with crack growth.

A direct current potential difference (d.c.p.d.) technique was used to record crack growth. To perform this technique, a pair of output potential wires were spot-welded on opposite edges of the notch and another pair of current wires were spot-welded on the top and bottom surfaces of the CT testpiece (at mid-width and mid-thickness) as suggested in ASTM E647 [8]. An in-house calibration function was generated with a series of potential values and crack length correlations obtained by running a test using an identical testpiece in which a number of beachmarks were introduced and later measured on the fracture surface.

The maximum load in all tests was 8 kN, and fatigue crack growth resistance curves were measured within a ΔK range of 20 – 60 MPa$\sqrt{m}$. Cracks were not grown to catastrophic failure during testing at elevated temperatures. Thereafter, the furnace was switched off and testpieces were allowed to cool to room temperature before being fatigued at room temperature and then fractured open. Note that to fracture the remaining ligament a notch is introduced into the back-face of the testpiece before monotonic loading to plastic collapse (final failure) at room temperature. A series of tests were conducted to investigate the influence of microstructure, testpiece orientation, side-grooves, test temperature and environment. Testing conditions for all fatigue crack growth results in this paper are listed in Table 2.

After fracture, crack lengths were measured using a digital optical microscope from the fracture surface. An in-house crack length-potential calibration equation plus a linear correction using the starting and finishing crack length was used to convert potential difference values to crack lengths. The calibration function used is shown in Eq. 1:

$$a/W = 0.0226(V/V_0)^3 - 0.18413(V/V_0)^2 + 0.67636\,(V/V_0) - 0.25908 \quad (1)$$

where a is the crack length, W is the width of the CT testpiece, V is the measured potential and V_0 is a reference potential value. Note this equation is only suitable for the experimental setup in the current research, which may need modification for a different setup, e.g. testpiece geometry and locations of potential wires and current wires.

The initial and final crack lengths were measured and used for crack length calculation for each test. In all cases, good agreement was found between crack lengths calculated with this calibration function and actual crack lengths measured on fracture surfaces with differences smaller than 1%. Stress intensity factors for plain-sided and side-grooved CT samples, ΔK and ΔK_n respectively, were calculated using the following equations according to ASTM E647 [8]:

$$\Delta K = \frac{\Delta P}{B\sqrt{W}} \frac{2+\alpha}{(1-\alpha)^{1.5}} \left(0.886 + 4.64\alpha - 13.32\alpha^2 + 14.72\alpha^3 - 5.6\alpha^4\right) \quad (2)$$

$$\Delta K_n = \Delta K \sqrt{\frac{B}{B_n}} \quad (3)$$

where $\alpha = a/W$, ΔP is the load range, B is the overall specimen thickness and B_n is the net specimen thickness.

After each test, fractography was conducted using a scanning electron microscope (SEM) to identify crack growth mechanisms. To understand differences of fatigue crack growth mechanisms in air and vacuum, cross-sectional samples for transmission electron microscope (TEM) investigation were extracted from fracture surfaces after testing at 650 °C in air and vacuum, by using an FEI Quanta 3D dual-beam focussed ion beam (FIB) microscope. Both sites chosen were from a crack length that corresponded to a ΔK value of ~30 MPa$\sqrt{m}$. The TEM cross-sectional foils were extracted perpendicular to fracture surfaces and striations in order to view crack profiles. A Pt coating was used to protect the fracture surface from being milled away. To minimize the amorphous layer and any damage caused by FIB milling, final cleaning was conducted at 5 kV.

Table 2 – Summary of fatigue crack growth test conditions and results. A and *m* values are derived for *da/dN* and ΔK measured in units of mm/cycle and MPa$\sqrt{m}$ respectively.

Temperature	Environment	Testpiece ID	Microstructure	Orientation	Side-groove	A	m
550 °C	Air	B-1	Inhomogeneous	L-T	0.5 mm	5.4×10^{-9}	3.4
		B-2	Inhomogeneous	L-T	0 mm	4.7×10^{-9}	3.4
					Average	5.1×10^{-9}	3.4
550 °C	Vacuum	A-1	Uniform	L-T	0.5 mm	4.9×101.4^{-10}	3.9
650 °C	Air	B-3	Inhomogeneous	L-T	0.5 mm	5.4×10^{-8}	2.8
		B-4	Inhomogeneous	ST-L	1 mm	4.4×10^{-9}	3.6
		A-2	Uniform	L-T	0.5 mm	2.6×10^{-8}	3.1
					Average	2.3×10^{-8}	3.1
650 °C	Vacuum	A-3	Uniform	L-T	1 mm	3.3×10^{-10}	4.1
		A-4	Uniform	L-T	1 mm	1.4×10^{-9}	3.7
					Average	7.4×10^{-10}	3.9
750 °C	Air	B-5	Inhomogeneous	L-T	0 mm	2.7×10^{-6}	1.8
		B-6	Inhomogeneous	L-T	0.5 mm	4.3×10^{-6}	1.7
					Average	3.6×10^{-6}	1.7
750 °C	Vacuum	B-7	Inhomogeneous	ST-L	1 mm	7.0×10^{-9}	3.3

2.3. *In-situ SEM fatigue crack growth testing at 750 °C*

In addition to testing using CT testpieces, a fatigue crack growth test (using a single-edge-notched testpiece under tension) was conducted at 750 °C in-situ within an SEM. Fig. 3 shows the setup of the heating and loading stage produced by Kammrath & Weiss GmbH inside the SEM chamber and a drawing of the dog-bone testpiece used. The width and thickness of the gauge section of this single-edge-notched dog-bone testpiece are 5 and 1 mm respectively. This testpiece was extracted in the L-T orientation. One surface of the dog-bone testpiece was ground and polished for SEM observation. The testpiece was notched and fatigue precracked at room temperature. After precracking, the entire gauge section of the polished surface was ion-milled in order to produce a surface appropriate for EBSD mapping. The last step in sample preparation was to coat the sample surface with a thin layer of Au-Pd (~3.8 nm) to protect the sample surface from oxidation during high temperature testing in the SEM. Further details of the setup of this in-situ testing can be found elsewhere [7].

Prior to applying heating or loading, an EBSD map was acquired over a large area ahead of the fatigue precrack. The sample was then heated to 750 °C in three steps all with a heating rate of 25 °C/min: first heated to 100 °C followed by a 5 min hold to allow any water vapour to outgas; then, to 300 °C followed by a 5 min hold to eliminate any organic solvents used during prior cleaning; and finally to the target temperature of 750 °C.

Once the temperature is stabilized at 750 °C, constant stress range fatigue loading was applied with R = 0.1. Due to the limited cycling capacity of the loading stage, the fatigue waveform used was a 3-1-3-1 trapezoidal (3 s each to reach the maximum or minimum load and 1 s hold at maximum and minimum loads). The ΔK range studied is similar to that applied to the CT samples. During the test, fatigue loading was paused at minimum load every 10 cycles to allow imaging of the crack path on the top surface of the sample and to observe any microstructural changes. Meanwhile, crack length was measured incrementally using reference points which were used to calculate crack growth rates and stress intensity factor range, ΔK. The appropriate stress intensity factor range, ΔK, was calculated using the equation below [9].

$$\Delta K = \frac{\Delta P}{BW}\sqrt{\pi a}\left[1.12 - 0.231\left(\frac{a}{W}\right) + 10.55\left(\frac{a}{W}\right)^2 - 21.72\left(\frac{a}{W}\right)^3 + 30.39\left(\frac{a}{W}\right)^4\right] \quad (4)$$

where same as before a is crack length, B and W are the thickness and width of the testpiece, and ΔP is the applied load range. Note that the equation is considered valid to a/W ≤ 0.6.

3. Results and discussion

3.1. *Fatigue crack growth resistance curves*

3.1.1. *Validity of ΔK*

The empirical relationship proposed by Paris and Erdogan [10] between the fatigue crack growth rate (da/dN) and the linear elastic stress intensity factor range (ΔK) has been the subject of much research and is widely used for defect tolerance design and lifing. This power-law relationship can be written as

$$\frac{da}{dN} = A(\Delta K)^m \quad (5)$$

where A and m are often termed Paris constants.

Obviously, a successful application of this correlation is based on the validity of ΔK, which is developed upon small scale yielding condition. However, one characteristic of fatigue crack growth in austenitic stainless steels is the large cyclic and monotonic plastic zone size ahead of the crack tip due to their low yield stress (typically ~200 MPa) at both room temperature and elevated temperatures. For Alloy 709 investigated in the current study, the size of the monotonic plastic zone is

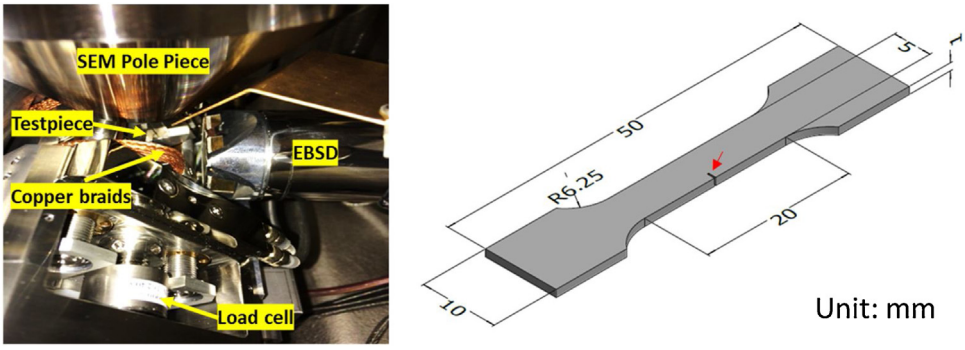

Fig. 3 – Photo of the heating and loading stage inside the SEM chamber and a schematic drawing of the flat dog-bone testpiece used. The red arrow indicates the notch.

estimated to exceed 1 mm in radius even at a ΔK of 20 MPa$\sqrt{m}$ (K_{max} = 22.2 MPa$\sqrt{m}$) using Irwin's approach, see Eq. 6.

$$r_p = \frac{1}{2\pi}\left(\frac{K}{\sigma_y}\right)^2 \quad (6)$$

Hence, although it is questionable whether small scale yield criteria required for using ΔK can be justified, and despite the extensive plasticity involved with the fatigue crack growth process, many authors have found that a linear elastic fracture mechanics (LEFM) based analysis can still describe crack growth rates in austenitic steels [11,12]. A comprehensive review and analysis on the validity of different fracture mechanics parameters including ΔJ-integral, crack tip opening displacement (CTOD) and ΔK was reported by Ljustell [13]. Using finite element computations and in-situ experiments Ljustell found the CTOD range (ΔCTOD) was able to characterise and correlate fatigue crack growth rates across small scale yielding to large scale yielding in an austenitic stainless steel (316 L). He also suggested ΔK could predict the growth rates due to marked isotropic work hardening under cyclic conditions and in the absence of crack closure. Such studies give some confidence that ΔK may be used to study fatigue crack growth resistance in Alloy709. Fig. 4 shows measured da/dN against ΔK in the log-log form for all tests in the current research. Indeed, a good Paris correlation (i.e. power law) between da/dN and ΔK can be found in all tests conducted.

3.1.2. *Side-grooving*

Before discussing the influence of microstructure, orientation, test temperature and environment, the treatment of side-grooving is worth addressing since CT testpieces used in the current research were sometimes plane-sided or had side-groove depths of either 0.5 or 1.0 mm (on each side). Crack growth in CT testpiece without side-grooves tends to bow due to different levels of plastic constraint from plane-strain (mid-section) and plane-stress (near-surface) regions across the testpiece thickness. This bowing effect is more prominent for crack growth under creep conditions [14]. Therefore, side-grooves are normally introduced to reduce uneven crack growth through thickness for creep crack growth tests. As for crack growth under fatigue loading, it is generally found that the use of side-grooves is unnecessary to promote uniform crack growth through-thickness and which indeed is found for plane-sided testpieces in the current study (see Fig. 5). It can be also seen in Fig. 4 that fatigue crack growth resistance curves from plane sided testpieces and testpiece with 0.5 mm deep side-grooves at the same temperature are found to overlap closely, such as B-1 and B-2 at 550 °C; B-3 and B-4 at 650 °C B-5 and B-6 at 750 °C. Note that Eq. 3, which is used to account for the influence of side-groove depths on the effective stress intensity factor, is recommended by ASTM E647 [8]. Relevant theoretical analysis and experimental verification for such a treatment can be found in [15,16].

3.1.3. *Effects of orientation and microstructure*

In Fig. 4b, fatigue crack growth resistance measured for different testpiece orientations at 650 °C in air (L-T and ST-L orientations drawn from the 32 mm thick plate and the 20 mm thick plate respectively) are compared. L-T and ST-L orientations are expected to demonstrate the largest variation if crack growth resistance is sensitive to testpiece orientation. As can be seen from Fig. 4b, crack growth resistance curves from B-3 and B-4 overlap, indicating that high temperature fatigue crack growth rates in Alloy 709 studied here are insensitive to testpiece orientation. It can also be deduced from Fig. 4b that any effect of a banded inhomogeneous microstructure is limited in these tests.

3.1.4. *Effects of test temperature and environment*

Since the influence of side-grooving, microstructure and testpiece orientation appears to be minimal, fatigue crack growth resistance curves (da/dN versus ΔK) obtained from different conditions can be compared directly. For each test, Paris constants *A* and *m* in Eq. 5 are given in Table 2. As can be seen, for tests with the same test condition (temperature and environment), both *A* and *m* values are very similar. Therefore, average values for these Paris constants are also determined for each test condition (where more than one test was carried out) by combining data from tests as one population. These average values are later used in developing an analytical model for fatigue crack growth in Alloy 709.

From Fig. 4, it is apparent that at the same temperature fatigue crack growth rates (da/dN) in air are generally higher than those measured in vacuum when compared at the same ΔK value. The differences between resistance curves in air and

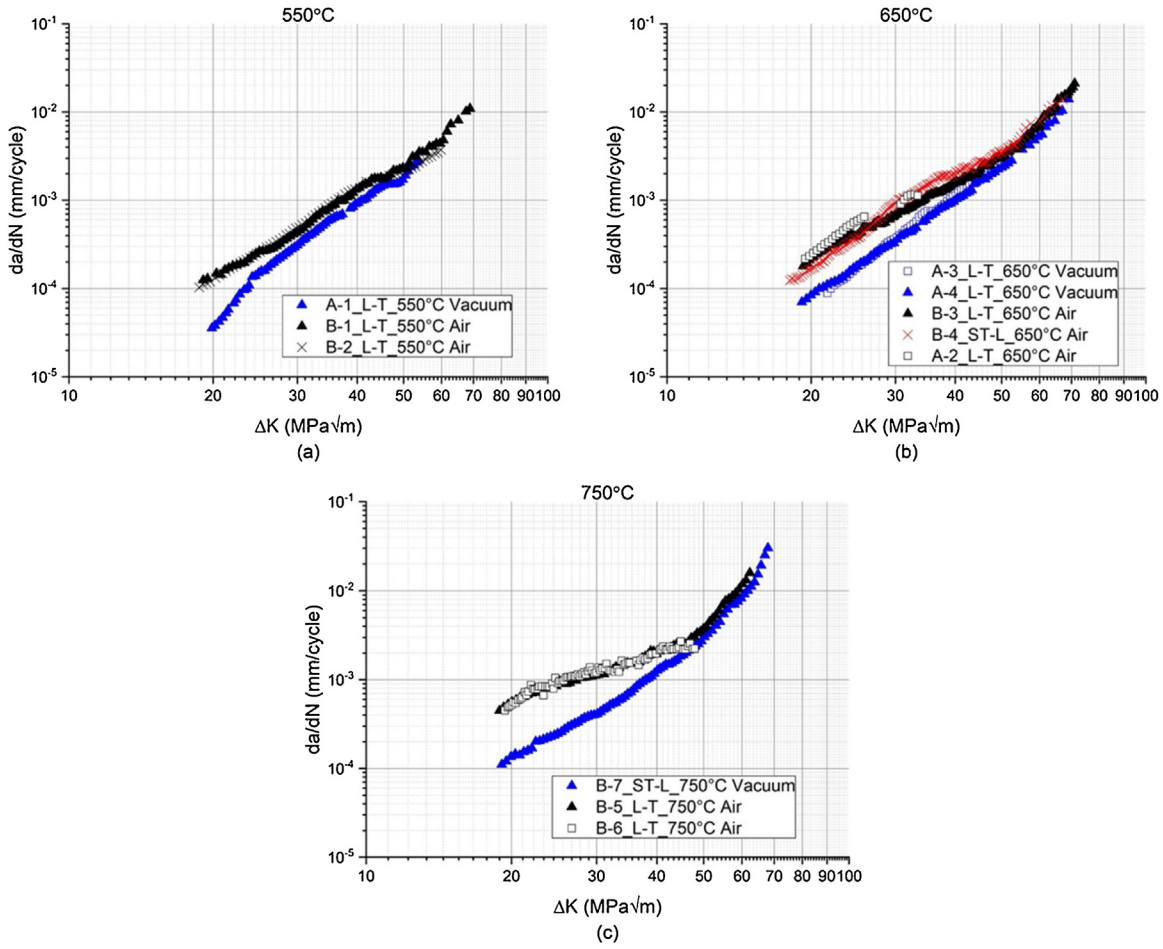

Fig. 4 – Fatigue crack growth resistance curves in Alloy 709 tested at different temperatures.

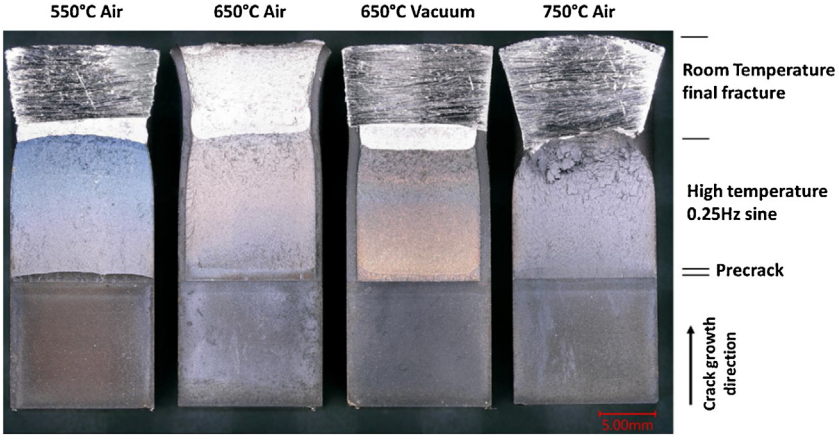

Fig. 5 – Representative optical images of fracture surfaces after testing at different temperatures.

in vacuum are increased at low ΔK values, become smaller at higher ΔK values and converge at ΔK values of ~ 50 to 60 MPa$\sqrt{m}$. This produces larger *A* values and smaller *m* values in the Paris equation for the tests conducted in air, comparing to those tested in vacuum (see Table 2). The differences between fatigue crack growth curves from air tests and vacuum tests clearly indicate a detrimental effect of air on the fatigue crack growth resistance of Alloy 709 at elevated temperatures under a frequency of 0.25 Hz. Similar observations have been previously reported for other austenitic stainless steels [17–19]. It also can be seen that with an increase of testing temperature, the differences in da/dN values in tests in air and vacuum increases. For example, at a ΔK value of 20 MPa$\sqrt{m}$, the crack growth rate in air is approximately twice that in vacuum at 550 °C, and this difference as a result of the test environment increases four-fold at 750 °C.

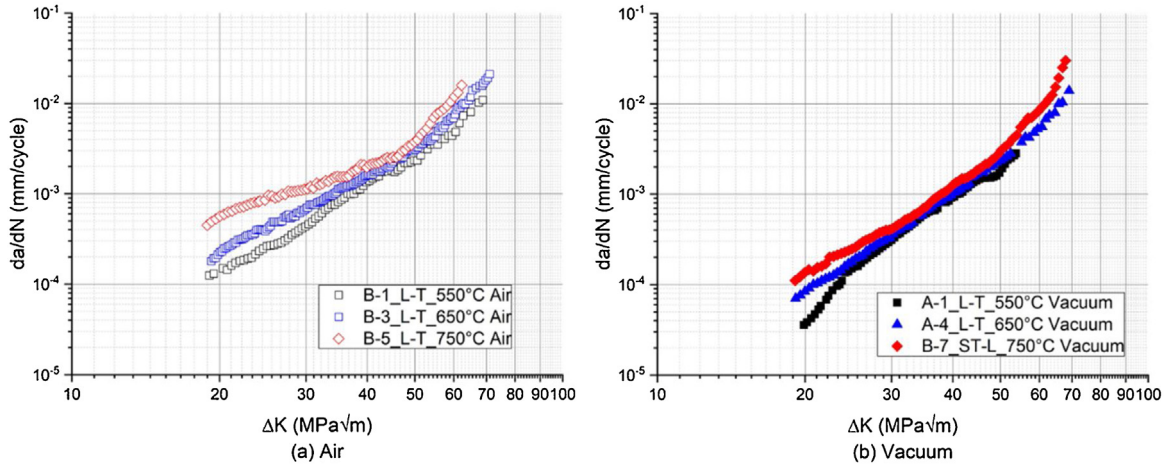

Fig. 6 – Effects of temperature on fatigue crack growth resistance in air and vacuum environments.

In Fig. 6, fatigue crack growth curves are re-arranged to compare the results obtained at different temperatures in vacuum and in air. Now it can be seen that the fatigue crack growth resistance curves from tests conducted in vacuum are all close together with only small differences at lower ΔK values between 550, 650, and 750 °C. In contrast, fatigue crack growth resistance curves in air are clearly different, most noticeably at these lower ΔK values. Moreover, fatigue crack growth rates are found to be faster for tests conducted at higher testing temperatures.

As for the detrimental effect of air environment on fatigue crack growth in Alloy 709 from 550–750 °C, hydrogen embrittlement can be ruled out [20]. It is likely that the accelerated crack growth rates observed here are associated with oxidation and/or oxygen embrittlement as other researchers have suggested [17–19]. These processes are all temperature-dependent, which means higher temperatures should accelerate the damage from the air environment and can plausibly explain the faster fatigue crack growth in air at higher temperatures seen here. It is worth noting that the role of the oxidizing environment on influencing fatigue crack growth rates may vary in different crack growth regimes [21].

3.2. *Fractography*

Representative optical images of fracture surfaces in Fig. 5 show that all fracture surfaces appear to be flat for the majority of fatigue crack growth. They become rougher when ΔK value exceeds ~50 MPa$\sqrt{m}$, which is also accompanied by the reduction of section thickness. Moreover, the roughness of the fracture surface increases with an increase of temperature.

SEM fractographs were taken at mid-thickness of each testpiece at locations of four different ΔK values (22, 30, 45 and greater than 50 MPa$\sqrt{m}$). Representative SEM fractographs from tests at 650 °C in both air and vacuum are shown in Fig. 7. It was found that fracture surfaces from all testing conditions, regardless of temperature, environment and orientation, are broadly similar and the dominant failure mechanism can be determined to be striated transgranular crack growth with the crack growth direction mostly close to mode I.

Up to ΔK values of 50 MPa$\sqrt{m}$, fatigue striations were found to cover the majority of the fracture surface, again in all tests, which suggests a cycle-by-cycle crack growth mechanism. It is also found that not only are the fracture surfaces from air tests generally slightly rougher than those from tests in vacuum, but fatigue striations are also more distinctive on the fracture surfaces from tests in air (e.g. as shown in Fig. 7c and g). Fig. 8 shows high magnification fractographs taken at ΔK of 30MPa$\sqrt{m}$ from testpieces tested in air at 550, 650 and 750 °C. Fatigue striations are well defined and their spacings are measured to be about 0.42, 0.81 and 1.24 μm respectively from Fig. 8. Such measured striation spacings match well with the average da/dN value shown in crack growth resistance curves measured using the d.c.p.d. method, which suggests values of 0.43, 0.91 and 1.20 μm/cycle respectively (see Fig. 6). In contrast, it was difficult to measure fatigue striations from vacuum tests as they are less distinct. Moreover, as measured values were often found to be inconsistent with da/dN at corresponding ΔK value. Such difficulty in measuring fatigue striations from tests in vacuum has been already recognized [22,23], and this is discussed further in section 3.4.

At high driving forces (ΔK > 50 MPa$\sqrt{m}$), although fatigue striations still dominate at 550 °C in both air and vacuum tests (see Fig. 9a and b), microvoids and secondary cracks start to appear. At 650 and 750 °C (Fig. 9c and d), fatigue striations are rarely seen in both air and vacuum tests at 750 °C (Fig. 9e and f), where dimples of different sizes now dominate the fracture surface. Formation of these dimples reflects severe plastic deformation due to increased net-section stresses and plastic collapse occurs. This is also evident from the observation of a reduction of section thickness as shown in the optical graphs in Fig. 5.

3.3. *In-situ SEM fatigue crack growth at 750 °C in vacuum*

Fig. 10 shows the fatigue crack growth resistance curve obtained from the in-situ SEM test at 750 °C (3-1-3-1 trapezoidal waveform, R = 0.1) together with data from a CT testpiece tested in vacuum (0.25 Hz sinusoidal waveform,

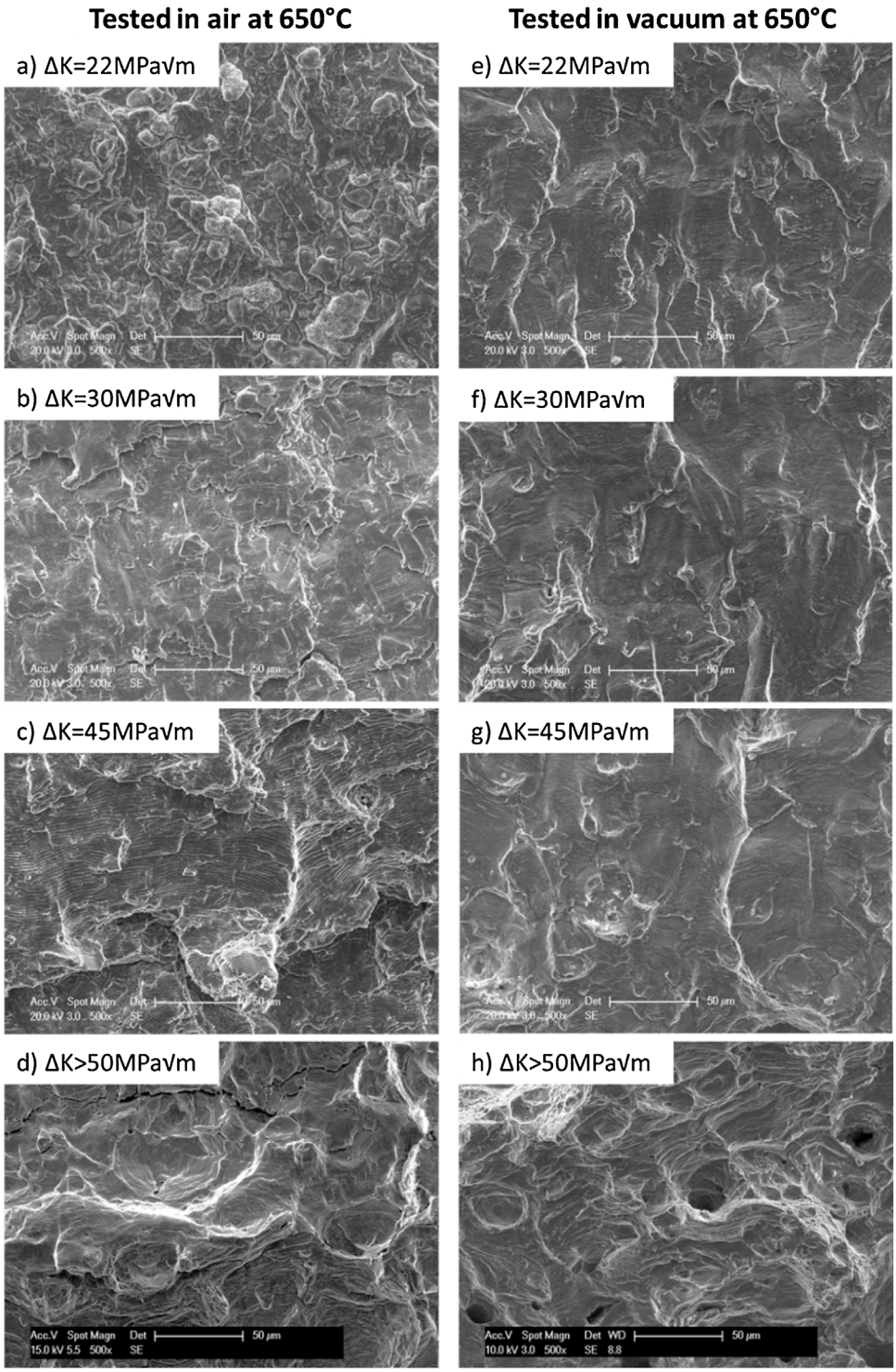

Fig. 7 – Representative SEM fractographs at different ΔK values after testing at 650 °C in air and vacuum.

R = 0.1). Reasonable agreement has been achieved between these two different specimen geometries and tests, although fatigue crack growth rates measured in the dog-bone in-situ test are generally slower. This discrepancy is likely to be attributed to the smaller testpiece size (1 mm versus 13 mm in thickness) and different loading configuration due to different sample geometry used (uniaxial tension in the dog-bone testpiece versus combined tension and bending in the CT testpiece). The influence of slower loading rate and multiple interruptions in the in-situ SEM test is believed to be minimal. That slower fatigue crack growth rates can be obtained from thinner test-pieces has been reported by other researchers [24].

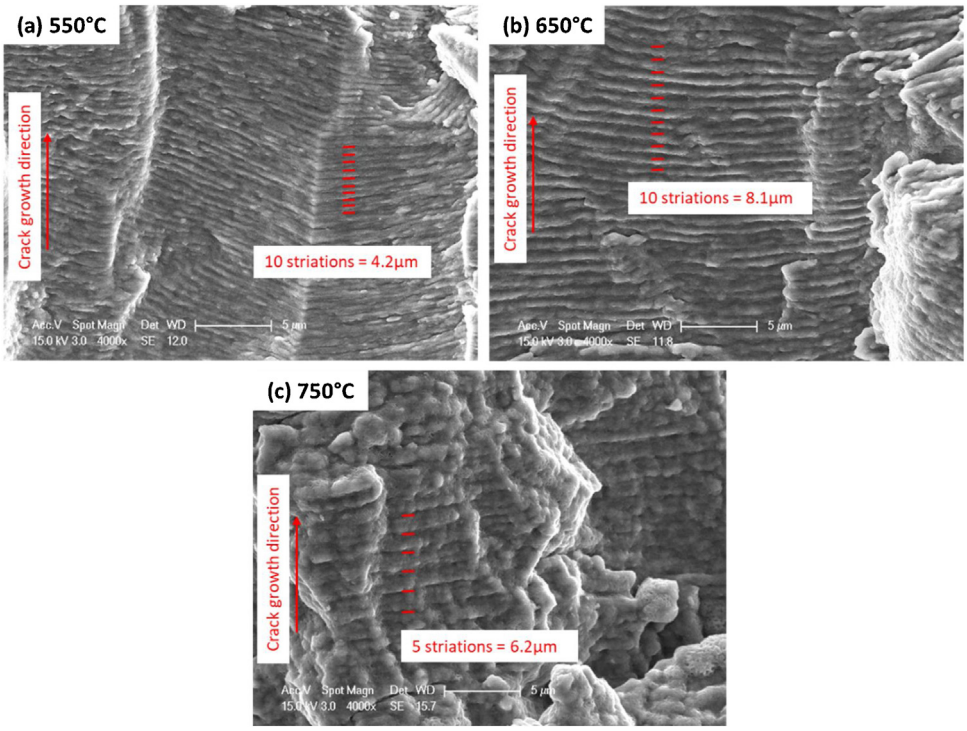

Fig. 8 – SEM fractographs of Alloy 708 tested in air at 550, 650 and 750 °C showing fatigue striations and corresponding measurements at $\Delta K = 30$ MPa$\sqrt{m}$.

Fig. 11 shows a secondary electron image and an EBSD map taken during the in-situ SEM fatigue testing up to ΔK =14.5 MPa$\sqrt{m}$. It can be confirmed from the image and particularly so from the EBSD map with a projected crack path (Fig. 11b) that the crack growth is primarily transgranular. Profuse slip bands can be found in the SEM micrographs (Fig. 11a) in a large area surrounding the crack tip. They appear as parallel lines on the sample surface. It is understood that these slip bands result from monotonic and cyclic deformation, and the extent of them is likely to relate to the monotonic plastic zone size. Although more than one slip system is likely to be activated in the Paris regime, only one direction is most visible. This suggests that this set of slip lines belongs to the dominant slip system. Close-up views of the slip bands at the current crack tip (region "1" in Fig. 11a) and when the crack was shorter (region "2" in Fig. 11a) are shown in Fig. 12. It is observed that the crack can grow either parallel to the slip bands (Fig. 12a), or by intercepting them (Fig. 12b), presumably following a secondary slip system. Note that the grains in the two areas which showed different slip directions have different orientations. It is believed these two scenarios could lead to the different appearance of "striation spacings" which will be discussed later.

3.4. *Mechanisms of fatigue crack growth in vacuum and air*

The most distinct characteristics of fatigue crack growth in the current research in Alloy 709 at elevated temperatures is the formation of fatigue striations on a flat transgranular crack path growing in the mode I direction, which are the dominant features here in both vacuum and air tests. Naturally, attempts were made to correlate average fatigue crack growth rates measured from testing with local crack growth rates measured from the striations observed on the fracture surfaces. For the fracture surfaces of the tests conducted in air, striations are easy to identify and good agreement is found throughout the ΔK range investigated, as shown in Fig. 8. On fracture surfaces of the tests conducted in vacuum and particularly at lower ΔK values, the striations found are finer and lack both definition and do not appear to be continuous. This makes both counting and accurate measurements difficult. Another interesting observation is that depending on which areas is examined, two sets of parallel lines of very different spacings can be seen, as shown in Fig. 13 and Fig. 14. In Fig. 13b ($\Delta K = 22$ MPa$\sqrt{m}$, 650 °C, vacuum), the spacing of the coarse lines on the bottom right area are about 1 μm, which is approximately seven times the average crack growth rate (da/dN) measured, see Fig. 4. The fine line features on the left of the micrograph seem perhaps to relate more to the average cyclic crack growth rates measured, but it is very difficult to count the number of striations within a known distance with confidence due to the lack of morphological contrast. At a ΔK value of 45 MPa$\sqrt{m}$ tested at 650 °C in vacuum, now these regions of finer spacings can be observed more clearly (Fig. 14b). On the close-up views in Fig. 14b, the width of coarse parallel lines on the right half is measured to be 1.8 μm which is consistent to the measured crack growth rate, however, a finer spacing can be seen on the left region.

The value of da/dN measured by d.c.p.d. is an overall average of crack growth rates over the whole crack front, while local crack growth rates (at each position of the crack front)

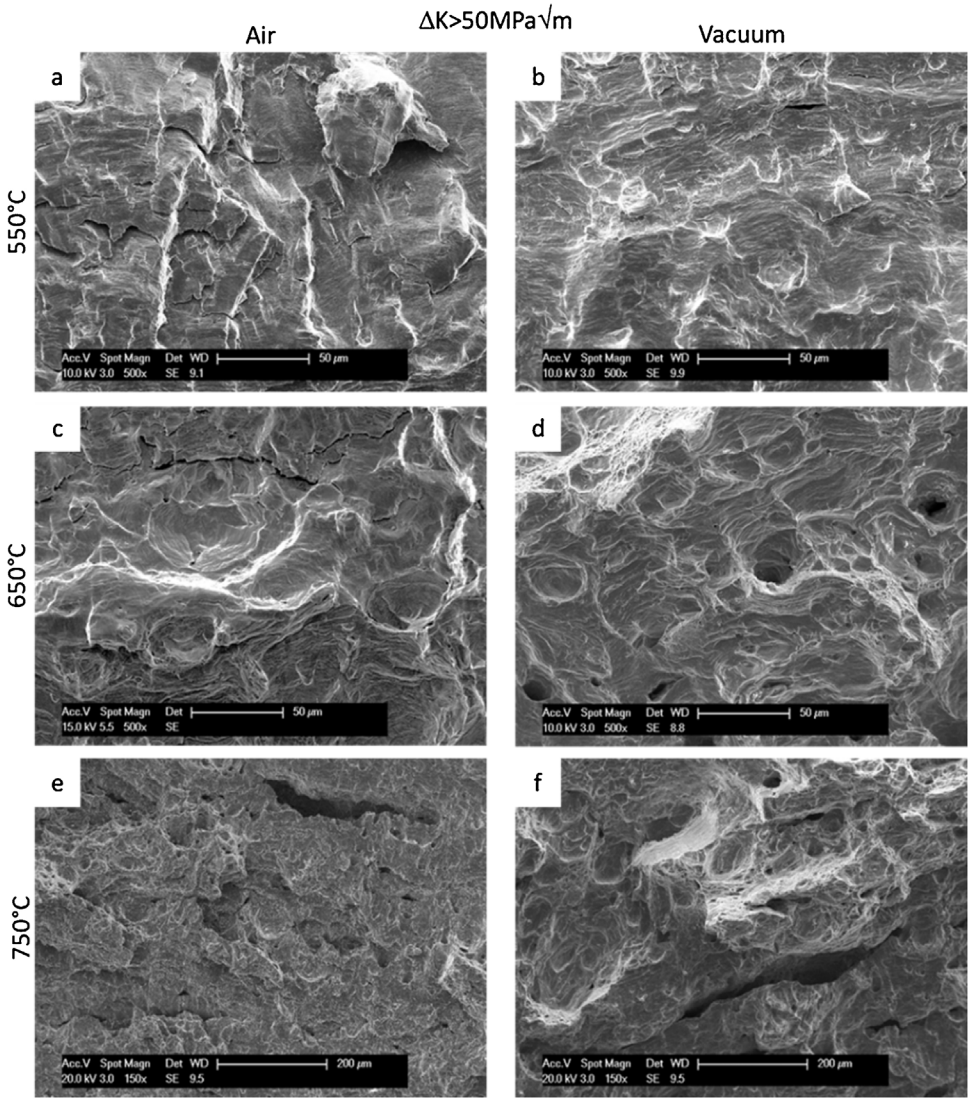

Fig. 9 – SEM fractographs in Alloy 709 tested at 550, 650 and 750 °C at $\Delta K > 50$ MPa$\sqrt{m}$.

may be different depending on the local grain orientation. In such cases, fatigue crack growth rates across the same crack front may vary. Besides this possibility, for different striations observed on the fracture surface (as shown in Fig. 14), it is also plausible that some of the parallel lines seen do not result from cyclic crack advance. Two types of striation spacing are also reported by Tomkins in Type 316 and 304 stainless steels [25]. Despite the observation of abnormal "striations" in vacuum, it is logical to consider that the fatigue crack growth mechanisms in vacuum and air are fundamentally the same, and the fatigue striations are formed by repeating a crack blunting and re-sharpening process, i.e. every individual cycle produces a mark on the fracture surface, hence da/dN equals to one striation spacing for the ΔK range investigated.

In-situ fatigue testing of the flat dog-bone sample in SEM at 750 °C provides some clues for possible mechanisms involved in forming additional abnormal "striation" which are not related to crack growth. The measurements of such "striations" seem to agree with the spacing of slip bands seen on the sample surface. While the spacing of fatigue striations

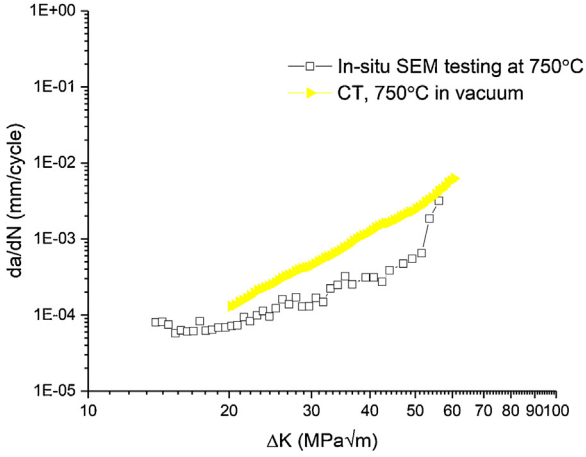

Fig. 10 – Comparison of fatigue crack growth resistance curves obtained from a CT testpiece and a flat dog-bone testpiece tested at 750 °C in vacuum.

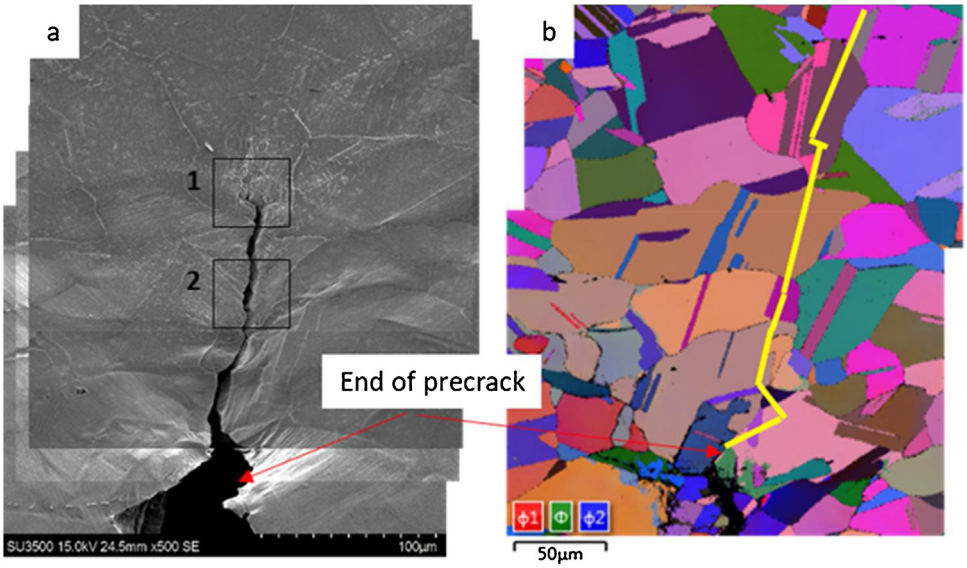

Fig. 11 – Secondary electron image (a) and EBSD Euler map of the flat dog-bone sample acquired at room temperature before testing (b) showing transgranular crack propagation for the in-situ SEM test. The yellow lines projected on the EBSD map indicate the crack growth path.

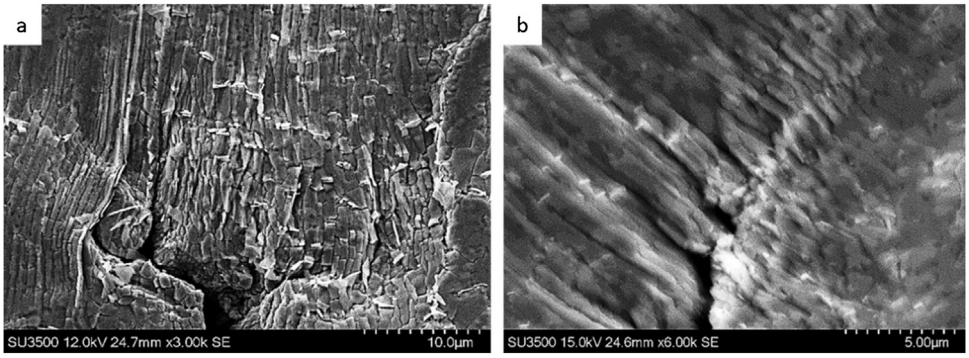

Fig. 12 – High magnification secondary electron images showing the slip traces of a) region 1 and b) region 2 noted in Fig. 11.

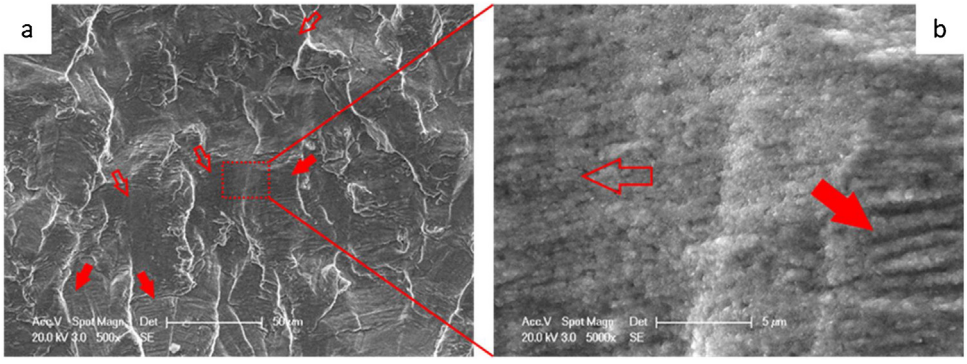

Fig. 13 – Fracture surface morphology and fatigue striations at a ΔK value of 22 MPa$\sqrt{m}$ from the test conducted at 650 °C in vacuum. Hollow arrows indicate flat areas with fine lines; solid arrows indicate areas with coarse lines.

increases with increasing crack length and ΔK, very small changes are seen to the spacing of such abnormal "striations". As mentioned before, these slip bands are observed in a relatedly large area around the crack tip and could be related to the dominant slip system(s) within the plastic zone. High magnification SEM images show that the crack can grow on these slip planes (parallel to slip bands on the surface, as shown in Fig. 12a), and sometimes it can grow across the slip planes (as shown in Fig. 12b), depending on grain orientation. When slip bands interact with the crack plane, steps may form in a regular manner. Such abnormal "striations" are rarely seen in tests carried out in air. This could simply because striations formed

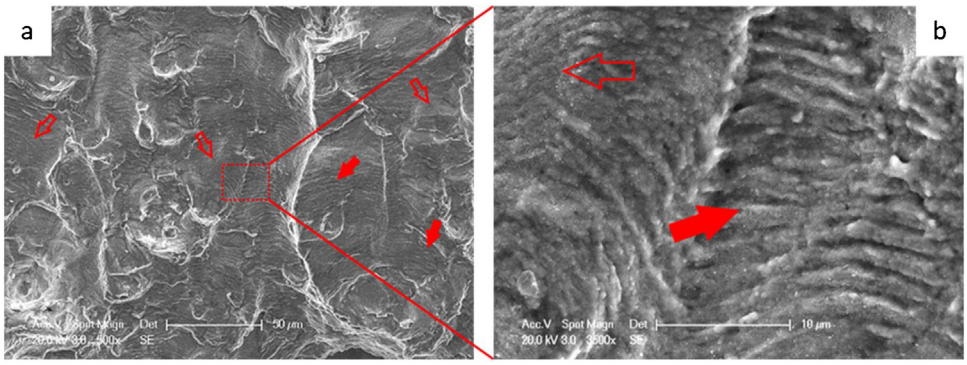

Fig. 14 – Fracture surface morphology and fatigue striations at a ΔK value of 45 MPa√m from the test conducted at 650 °C in vacuum. Hollow arrows indicate flat areas with fine lines; solid arrows indicate areas with coarse lines.

in air are far deeper than any lines produced by intercepting slip traces.

In order to further understand the mechanism, two cross-section TEM samples were lifted out from the fracture surfaces of CT testpieces tested at 650 °C in air and vacuum respectively. The chosen sites were both at a crack length that gives a ΔK of ~30 MPa√m. As shown in Fig. 15a and c, TEM foils were extracted parallel to the crack growth direction (perpendicular to the striations) aiming to compare crack profiles formed in air and vacuum environments. Bright field STEM image of the two samples are shown in Fig. 15b and d.

Both crack surfaces are covered by an oxide layer despite one being tested in vacuum. TEM-EDX analysis confirms Fe-, Cr- and Si-rich oxides for both the air and vacuum samples. As commonly observed in austenitic stainless steels, the outer layer of the scale is a Fe-rich oxide with an inner layer consisting of a Cr-rich oxide, and discontinuous Si-rich oxides seen between the Cr-rich oxide and the matrix. However, oxides formed in air are denser and more continuous. It is considered that the oxide scale seen in both samples formed due to prolonged exposure at temperature after the crack had propagated. For a growing crack under fatigue loading in terms of the current study at 0.25 Hz, it is considered reasonable to assume the initial oxidation rate at the freshly-exposed crack tip is higher in air than in vacuum due to the higher oxygen partial pressure and hence faster transport of oxygen. The nature of this initial oxidation damage within each cycle completed in four seconds is difficult to characterise experimentally. However, some form of additional environmental damage in air can be deduced which affects both fatigue crack growth rates and the morphology of striations.

As shown in Fig. 15b, for the sample drawn from the fatigue crack growth test conducted in air, repeating "peaks" and "valleys" can be identified with confidence. The spacings between the adjacent "valleys" match with the average crack growth rates per cycle measured using d.c.p.d. method (see Fig. 4) and the striation spacing measured from fracture surface (see Fig. 8), which are all around 0.8 μm at this particular crack length (ΔK ~ 30 MPa√m). In contrast, the test in vacuum has produced a very flat crack path with little evidence of any "peaks" and "valleys".

TEM micrographs of these two samples also reveal a layer of very fine equiaxed grains of 100–300 nm in size immediately beneath the fracture surface which lies on top of a lamellae-like substrate which is of ~50–250 nm in width and contains high-density dislocations. These lamellae are found to have very similar orientations with [110] roughly aligned parallel to the loading direction for both cases (see inserts in Fig. 15b and d for selected area diffraction patterns for the lamellae-like regions in each sample). This implies severe deformation and local fracture occurred around the crack tip. Such band-like microstructures have been found in, for example, S304H steel after being rolled to a total strain of 200% at 500 °C [26]. These equiaxed fine grains are believed to result from recrystallization but it is not clear when recrystallization occurred. It is thus very likely that it was due to severe plastic deformation locally. The curvature of the lamellar structure towards the crack face and the greater degree of recrystallization seen in the sample tested in vacuum are deduced to due to a larger degree of blunting (plastic deformation), compared to the air sample, which had then been subsequently compressed upon reducing load to the minimum load.

Fatigue crack growth extension in air and in vacuum is proposed to occur over a fatigue cycle as follows:

a) At the minimum load of a fatigue cycle, the crack opening is very small and crack faces just behind the crack tip may be in near contact depending on the minimum load.
b) During load increase the crack opens. In vacuum tests, no crack extension is considered to happen during the early stages of load increase with only crack tip blunting occurring due to the high stresses local to the crack tip. In air tests, it is proposed that localised environmental damage (oxidation) can occur rapidly on freshly exposed surfaces as the crack opens. Due to this damage, earlier crack advance, $\left(\frac{da}{dN}\right)_1$, is postulated to happen ahead of that which will occur in vacuum.
c) As the load continues to increase towards its maximum over the cycle, crack advance is postulated to happen both in air and in vacuum. This will lead in vacuum to a crack increment of $(\frac{da}{dN})_{vac}$ and a further crack increment in air of $\left(\frac{da}{dN}\right)_2$. In air if this further increment is considered to be in non-damaged material then it is plausible that this increment could to closely similar to that observed in vacuum $(\frac{da}{dN})_{vac}$. Now, crack growth steps are completed over a

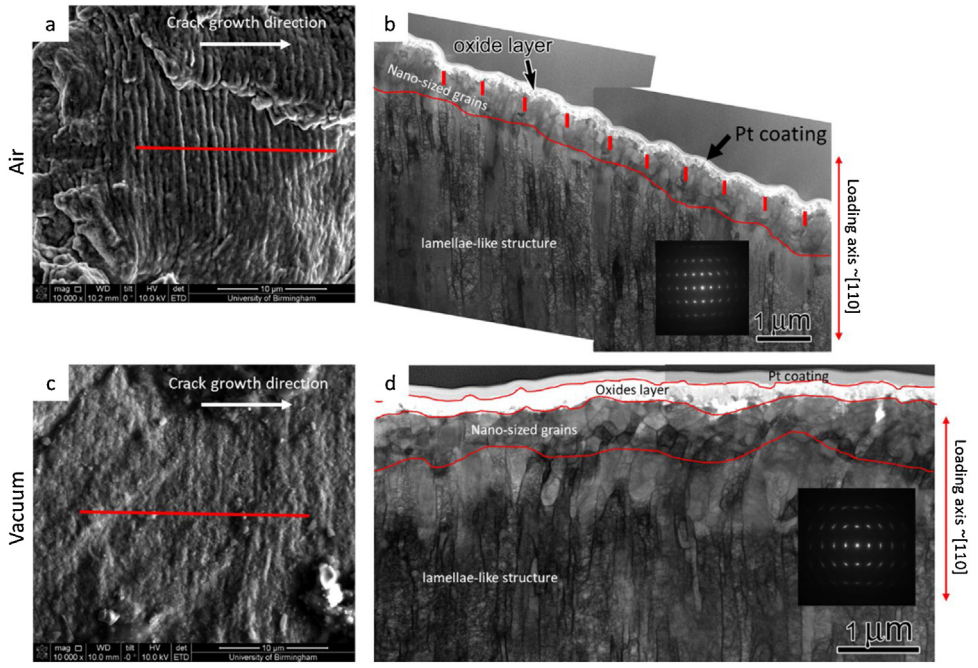

Fig. 15 – SEM fractographs of testpieces tested at 650 °C in air (a) and vacuum (c) at ΔK of ~30 MPa√m showing where the TEM sample was extracted using a FIB; and BF-STEM images showing cross-section views of TEMs sample extracted in air (b) and vacuum (d).

fatigue loading cycle and the total crack growth in a single cycle in air, $\left(\frac{da}{dN}\right)_{air}$ is the summation of $\left(\frac{da}{dN}\right)_1$ and $\left(\frac{da}{dN}\right)_2$.

d) During the load decreasing stage, cracks both in air and in vacuum tests start to close. Meanwhile, even though further crack advance may not happen, damage (oxidation) will continues to accumulate at the crack tip in air tests. Of note, it is considered that in air the difference in plastic strains required to produce initial crack advance, $\left(\frac{da}{dN}\right)_1$, into damaged material and subsequent crack advance, $\left(\frac{da}{dN}\right)_2$, into unaffected material will result in a ridge at the crack front. In vacuum, if it is accepted there is only one step in the crack advance, reverse loading would plausibly produce more uniform deformation which would form a smoother crack profile and indistinct fatigue striations as seen in Fig. 15b.

3.5. *Analytical model of fatigue crack growth in air*

According to the mechanism proposed in the previous section, fatigue crack growth per cycle in air at elevated temperatures for Alloy 709 can be divided into two parts:

$$\frac{da}{dN_{air}} = \frac{da}{dN_1} + \frac{da}{dN_2} \tag{7}$$

From the consideration above it follows that $\frac{da}{dN_2} \approx \frac{da}{dN_{vac}}$, Eq. 7 becomes:

$$\frac{da}{dN_{air}} = \frac{da}{dN_{vac}} + \frac{da}{dN_{en}} \tag{8}$$

where $\frac{da}{dN_{vac}}$ is the fatigue crack growth rate measured in vacuum tests, $\frac{da}{dN_{en}}$ is the crack growth part in each cycle due to environmental damage. The extent of environmental damage ahead of a fatigue crack tip in each cycle is a complex process as it should compose of oxygen diffusion, oxidation and separation of the "weakened material". Therefore, in detail it will depend on the test temperature and local stresses at and ahead of the crack tip.

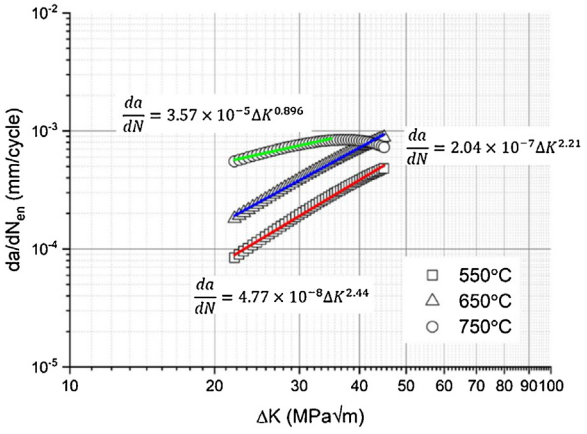

Fig. 16 – Calculated crack growth per cycle due to environmental damage ($\frac{da}{dN_{en}}$) at different ΔK values.

According to Eq. 8, $\frac{da}{dN_{en}}$ can be calculated by subtracting $\frac{da}{dN_{vac}}$ from $\frac{da}{dN_{air}}$. Fig. 16 shows $\frac{da}{dN_{en}}$ values from ΔK equals 22–45 MPa√m at different temperatures which are obtained by using the (average) Paris constants listed in Table 2. As shown in this log-log plot, except for ΔK > 35 MPa√m at 750 °C, $\frac{da}{dN_{en}}$ always increases with increase of ΔK at all temperatures, which illustrates a ΔK dependence of the environmental con-

tribution to crack growth. A possible reason for the different behaviour of $\frac{da}{dN}_{en}$ for $\Delta K > 35$ MPa$\sqrt{m}$ at 750 °C is that the failure mechanism deviates from striated transgranular crack growth alone to incorporate a degree of monotonic (plastic collapse) failure due to the severe degree of general plastic deformation. Therefore, this data are excluded here from the derivation of an analytical model for the Paris regime fatigue crack growth. In fact, if the range of ΔK is extended beyond 45 MPa$\sqrt{m}$ for tests at 550 and 650 °C similar considerations apply.

Since the crack growth rate thus is seen to depend on both ΔK and temperature, an analytical model for $\frac{da}{dN}_{en}$ must contain sufficient variables to capture both dependencies. One such attempt is given by Eq. 9 according to [27].

$$\frac{da}{dN}_{en} = c_0 exp\left(-\frac{Q}{RT}\right)\Delta K^{m_{0+}c_{1/RT}} \quad (9)$$

where c_0, m_0 and c_1 are temperature-independent constants, Q is the activation energy for high temperature environmental damage at the crack tip for the material studied here and R is the gas constant which equals to 8.314 J/mol/K. By comparing Eq. 9 with experimental data, the fits shown in Fig. 16 allow the temperature-independent constants and activation energy to be determined. Using m and A values for fatigue crack growth in vacuum at 550 °C, which are used to represent crack growth rates, $\frac{da}{dN}_{vac}$, in vacuum over the full temperature range of interest (see Fig. 5b) an overall equation for fatigue crack growth in Alloy 709 at elevated temperatures in air can be written as

$$\frac{da}{dN} = A\Delta K^m + c_0 exp\left(-\frac{Q}{RT}\right)\Delta K^{m_{0+}c_{1/RT}} \quad (10)$$

$$\frac{da}{dN} = 4.94\times10^{-10}\Delta K^{3.91} + \exp(15.52)\,exp\left(-\frac{226047}{RT}\right)\Delta K^{-5.04+52463/RT} \quad (11)$$

where the units of Q, c_1 are given in J/mol, the unit for T is in Kelvin, and other constants have been derived for da/dN and ΔK in units of mm/cycle and MPa$\sqrt{m}$ respectively.

Fig. 17 compares the experimental data measured with CT testpieces and results from this analytical model. As can be seen, experimental curves and this empirical model show very good agreement which suggests that this equation could certainly be used to predict fatigue crack growth rates in Alloy 709 at intermediate temperatures between 550 and 750 °C.

As shown in Eq. 11, the activation energy for high temperature fatigue crack growth in Alloy 709 at 550–750 °C is found to be 226 kJ/mol in the current study. The activation energy for the oxidation of 316 L stainless steel at 600–800 °C was measured to be 149 kJ/mol [28], while the activation energy for the oxidation of nickel-based superalloys ranges from 200 to 300 kJ/mol depending on the chemical composition [28,29]. Alloy 709 is regarded to have a better oxidation resistance than 316 stainless steels but may not be as good as nickel alloys. The value of 226 kJ/mol sits between the activation energy for oxidation measured in 316 and nickel alloys. This suggests that

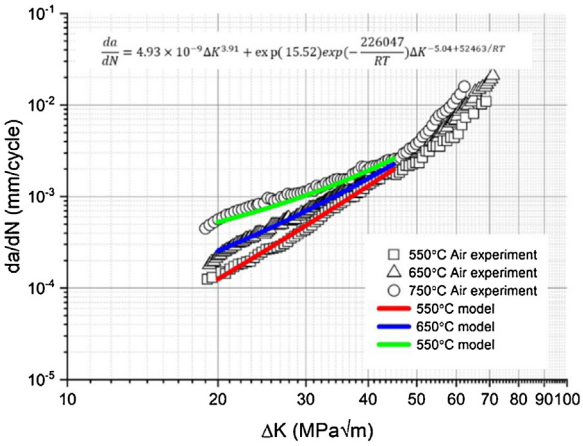

Fig. 17 – Experimental data and analytical model results for fatigue crack growth in Alloy 709 in air at different temperatures.

postulated environmental damage at the crack tip is indeed likely to be oxidation.

4. Conclusions

The fatigue crack growth resistance in the intermediate Paris regime for an austenitic stainless steel Alloy 709 has been investigated at temperatures of 550, 650 and 750 °C in both air and vacuum in the present study.

1) The fatigue crack growth resistance of Alloy 709 can be successfully described by stress intensity factor range, ΔK, despite the presence of "large" plastic zones at the crack tip.
2) For the temperature range studied, fatigue crack growth resistance of Alloy 709 in the vacuum environment was independent of temperature, but crack growth rates were accelerated to different degrees when tested in air. Modest increases in crack growth rates in air over those measured in vacuum were found to depend both on temperature and ΔK. Differences in fatigue crack growth resistance curves measured in air compared to those measured in vacuum are more marked both at higher test temperatures and at lower ΔK values. This dependency of crack growth rates in air on both temperature and ΔK makes predictions of crack growth rates in air from those measured in vacuum challenging. Nevertheless an empirical analytical model fitted from the experimental results appears to have some potential to predict fatigue crack growth rates in Alloy 709 when tested in air.
3) The principal failure mechanism under cyclic loading both in air and in vacuum is by transgranular striated crack growth. Local crack growth rates derived from striation spacings in air correlate closely with average crack growth rates measured using an electrical analogue method (direct current potential difference) and striations observed from tests in air are much more distinctive than those observed from tests in vacuum. Moreover, local crack growth rates derived from observations of apparent striations in vac-

uum do not always match with average crack growth rates measured by direct current potential difference. Care is needed to distinguish striations from slip traces observed on fracture surfaces produced from tests performed in vacuum.

Conflicts of interest

The authors declare no conflicts of interest.

Acknowledgements

This study is part of a project funded by the US Department of Energy (DOE) Nuclear Energy University Program (NEUP) award 2015-1877/ DE-NE0008451, and the UK Engineering and Physical Research Council award EP/N016351/1).

REFERENCES

[1] Nippon Steel & Sumitomo Steel, NF709 material data sheet. Http://www.tubular.nssmc.com/product-services/specialty-tube/product /nf709.
[2] Shaber N, Stephens R, Ramirez J, Potirniche GP, Taylor M, Charit I, et al. Fatigue and creep-fatigue crack growth in alloy 709 at elevated temperatures. Mater High Temp 2019;36(6):562–74.
[3] Wood D, Baldwin A. Creep/fatigue behaviour of type 316 steel in sodium, Specialist meeting on mechanical properties of structural materials including environmental effects; 1982.
[4] Mishra MP, Packiaraj CC, Ray SK, Mannan SL, Borgstedt HU. Influence of sodium environment and load ratio (R) on fatigue crack growth behaviour of a Type 316 LN stainless steel at 813 K. Int J Press Vessel Pip 1997;70(1):77–82.
[5] Ding R, Yan J, Li H, Yu S, Rabiei A, Bowen P. Deformation microstructure and tensile properties of Alloy 709 at different temperatures. Mater Des 2019;176.
[6] Ding R, Yan J, Li H, Yu S, Rabiei A, Bowen P. Microstructural evolution of Alloy 709 during aging. Mater Charact 2019;154:400–23.
[7] Upadhayay S, Li H, Bowen P, Rabiei A. A study on tensile properties of Alloy 709 at various temperatures. Mater Sci Eng A 2018;733:338–49.
[8] ASTM. Standard test method for measurement of fatigue crack growth rates; 2015.
[9] Tada H, Paris PC, Irwin GR. The stress analysis of cracks handbook. New York: ASME press; 2000.
[10] Paris P, Erdogan F. A critical analysis of crack propagation laws. J Basic Eng 1963;85(4):528–33.
[11] Thompson AW. Fatigue crack propagation in austenitic stainless steels. Eng Fract Mech 1975;7(1):61–8.
[12] Wareing J. Fatigue crack growth in a type 316 stainless steel and a 20 pet Cr/25 pet Ni/Nb stainless steel at elevated temperature. MTA 1975;6(7):1367.
[13] Ljustell P. Fatigue crack growth experiments on specimens subjected to monotonic large scale yielding. Eng Fract Mech 2013;110:138–65.
[14] He JZ, Wang GZ, Tu ST, Xuan FZ. Effects of side-groove depth on creep crack-tip constraint and creep crack growth rate in C(T) specimens. Fatigue Fract Eng Mater Struct 2018;41(2):260–72.
[15] Freed C, Krafft J. Effect of side grooving on measurements of plane-strain fracture toughness(Side grooving effect on measurements of plane strain fracture toughness). J Mater 1966;1:770–90.
[16] Macdonald B, Pajot J. Stress intensity factors for side-grooved fracture specimens. J Test Eval 1990;18(4):281–5.
[17] Sadananda K, Shahinian P. Effect of environment on crack growth behavior in austenitic stainless steels under creep and fatigue conditions. MTA 1980;11(2):267–76.
[18] Mills WJ, James LA. Fatigue crack propagation behaviour of type 316 stainless steel at elevated temperature in a vacuum. Int J Fatigue 1988;10(1):33–6.
[19] Mahoney MW, Paton NE. The influence of gas environments on fatigue crack growth rates in types 316 and 321 stainless steel. Nucl Technol 1974;23(3):290–7.
[20] Yagodzinskyy Y, Todoshchenko O, Papula S, Hänninen H. Hydrogen solubility and diffusion in Austenitic stainless steels studied with thermal desorption spectroscopy. Steel Res Int 2011;82(1):20–5.
[21] King J, Cotterill PJ. Role of oxides in fatigue crack propagation. Mater Sci Technol 1990;6(1):19–31.
[22] Grinberg NM. The effect of vacuum on fatigue crack growth. Int J Fatigue 1982;4(2):83–95.
[23] Wanhill RJH. Fractography of fatigue crack propagation in 2024-T3 and 7075-16 aluminum alloys in air and vacuum. MTA 1975;6(8):1587.
[24] Park H-B, Lee B-W. Effect of specimen thickness on fatigue crack growth rate. Nucl Eng Des 2000;197(1):197–203.
[25] Tomkins B, Biggs WD. Low endurance fatigue in metals and polymers. J Mater Sci 1969;4(6):539–43.
[26] Yanushkevich Z, Belyakov A, Kaibyshev R. Microstructural evolution of a 304-type austenitic stainless steel during rolling at temperatures of 773–1273K. Acta Mater 2015;82:244–54.
[27] Evans J. Environment assisted crack growth in nickel-base superalloys at elevated temperature, University of Arkansas; 2008.
[28] Us H. Oxidation behavior of very high temperature reactor (VHTR) candidate materials: 316l stainless steel, Alloy 617, and Incoloy-800H, University of Missouri—columbia; 2016.
[29] Cruchley S, Taylor MP, Evans HE, Hardy MC, Child DJ. Characterisation of subsurface oxidation damage in Ni based superalloy, RR1000. Mater Sci Technol 2014;30(15):1884–9.